

Effects of Solvents and Al Doping on Structure and Physical Properties of BiFeO₃ Thin Films

Xia-Li Liang

Kunming University of Science and Technology - Lianhua Campus: Kunming University of Science and Technology

Jian-Qing Dai (✉ djqkust@sina.com)

Kunming University of Science and Technology - Lianhua Campus: Kunming University of Science and Technology <https://orcid.org/0000-0003-4352-0789>

Chang-Chang Zhang

Kunming University of Science and Technology - Lianhua Campus: Kunming University of Science and Technology

Tian-Fu Cao

Kunming University of Science and Technology - Lianhua Campus: Kunming University of Science and Technology

Research Article

Keywords: BiFeO₃ thin films, Al doping, spin coating, physical property

Posted Date: October 8th, 2020

DOI: <https://doi.org/10.21203/rs.3.rs-86506/v1>

License: © ⓘ This work is licensed under a Creative Commons Attribution 4.0 International License.

[Read Full License](#)

Version of Record: A version of this preprint was published at Journal of Sol-Gel Science and Technology on February 23rd, 2021. See the published version at <https://doi.org/10.1007/s10971-021-05489-y>.

Effects of solvents and Al doping on structure and physical properties of BiFeO₃ thin films

Xia-Li Liang, Jian-Qing Dai*, Chang-Chang Zhang, Tian-Fu Cao

Faculty of Materials Science and Engineering, Kunming University of Science and Technology, Kunming 650093, PR China

*Corresponding author. Fax: +86 871 65107922.

E-mail address: djqkust@sina.com (J.-Q. Dai).

ORCID: 0000-0003-4352-0789 (Jian-Qing Dai)

ABSTRACT

In this study, structure, optical character, morphology, element-valence and characteristic ferroelectricity of BiFeO₃ (BFO) and BiFe_{0.96}Al_{0.04}O₃ (BFAO) thin films were investigated experimentally. BFO and BFAO thin films were prepared on fluorine-doped tin oxide (FTO) substrates via spin coating with two acid solvents. One solvent was aqueous solution of nitric acid (solvent I), and the other one was mixture of 2-methoxyethanol and glacial acetic acid (solvent II). X-ray diffraction (XRD) showed that films maintained their rhombic perovskite structures, which were *R*3c. Raman spectra showed that Al doping causes structural distortion. Al doping solves the problem of porosity and improves the density of BFO film. Average grain size of BFAO- II sample is about 110 nm, and, its thickness is the smallest (~714 nm). This indicates that BFAO- II sample is highly compact. Energy spectrum shows that Al has doped in the film, uniformly. X-ray photoelectron spectroscopy (XPS) shows that the presence of Al inhibited the floating of Fe valence. BFAO- II sample has excellent ferroelectricity ($2P_r \sim 110 \mu\text{C}/\text{cm}^2$), and leakage current density ($\sim 10^{-2} \text{ A}/\text{cm}^2$) is lower than that of undoped BFO film. Al doping can reduce the band gap width (E_g) of BFO films, specifically, values of E_g are 2.28 (BFO- I), 2.26 (BFO- II), 2.17 (BFAO- I) and 2.21 (BFAO- II) eV. This work provides new idea for the application of Al-doped BFO films in photocatalysis and photovoltaic devices.

Keywords: BiFeO₃ thin films, Al doping, spin coating, physical property

1. Introduction

At present, multiferroic materials are a research hotspot. Multiferroics could be

characterized by the possession of two or more ferroic order parameters, mainly including ferroelectric, ferroelastic, and ferromagnetic (antiferromagnetic). Multiferroic materials be endowed with fantastic physical effects via the coupling of these orders, mainly including magnetoelectric, magnetoelastic, and piezoelectric [1, 2]. Pb-based materials $\text{Pb}(\text{Zr}_{1-x}\text{Ti}_x)\text{O}_3$ (PZT) have been widely applied and commercially used in high-performance piezoelectric devices. Unfortunately, PZT devices that are Pd-based materials are not environmentally friendly [3]. Pb-free Bi-based materials are potential candidates for materials that can be substituted for Pb-based multiferroic materials. Multiferroic BiFeO_3 (BFO) is a typical Bi-based material, that possesses an excellent ferroelectric order (Curie temperature, $T_C \sim 830 \text{ }^\circ\text{C}$) and G-type antiferromagnetic order (Neel temperature, $T_N \sim 370 \text{ }^\circ\text{C}$). BFO can be used in high temperature magnetoelectric coupling devices [2].

BFO has always been a favorite topical of researchers, including in the forms of zero-dimensional powder [4, 5], one-dimensional fiber [6], two-dimensional film [7], and three-dimensional bulk [8]. These materials can potentially be used in photocatalysis, photovoltaics, phototransduction, energy harvesting devices, sensors, and actuators, because they have excellent photoabsorption and ferroelectric and piezoelectric properties [9-11]. However, the commercial production and application of BFO is hampered by its inherent problems, including high leakage, high loss, low polarization, valence floating (+2, +3, +4) of Fe, and associated phases (Bi-rich phases: Bi_2O_3 and $\text{Bi}_{25}\text{FeO}_{39}$, Fe-rich phases: $\text{Bi}_2\text{Fe}_4\text{O}_9$ and Fe_2O_3). Wang et al. [12] used rapid liquid phase sintering and prepared high quality BFO ceramics with a saturated hysteresis loop ($2P_r \sim 7.5 \text{ } \mu\text{C}/\text{cm}^2$), many researchers were inspired by this work. Spark plasma sintering (SPS) [13] and quenching [14] shorten dwell time at high temperature during heat treatment, and these methods are widely used to solve problems of impure phases in bulk ceramics. Much research have been conducted on substituting rare earth (RE) ions (La, Eu, Sm, Yb, Ho, etc.) for Bi, and it has been that found RE-doping can increase ferroelectricity because of structural distortion or emergence of morphotropic phase boundary (MPB) [15-19]. Kan et al. [20] found that rare earth ion doping in BFO thin films arise a common phenomenon. RE (Sm, Gd,

Dy) doping can cause structural distortion and lead to double hysteresis loops, because of the electric field-induced transition from paraelectric state to ferroelectric state. Synchronously, according to some literature transition elements (Mn, Zn, Ti, Al, etc.) are used to substitute for Fe to solve the problem of large leakage current [21-24].

Ferroelectric materials essentially have spontaneous electric polarization (P_s) below T_C [25]. Theoretical P_s values of BFO films are considerable ($\sim 150 \mu\text{C}/\text{cm}^2$). Unfortunately, saturated electric polarization loops (P-E loops) of BFO materials are obstructed to observe for poor quality and resistivity. The ferroelectric properties of thin film samples are generally better than those of bulk materials. In particular, for epitaxial BFO films, the electric polarization is directional, P_s values of [111] and [001] are observed to be $100 \mu\text{C}/\text{cm}^2$ and $65 \mu\text{C}/\text{cm}^2$, respectively [26]. Most notably, Zhang et al. [27] experimentally estimated P_s value of BFO epitaxial thin films with tetragonal phase that exceed $140 \mu\text{C}/\text{cm}^2$ under a high test electric field ($\sim 1000 \text{ kV}/\text{cm}$). Perovskite BiAlO_3 (BAO) which has $R3c$ symmetry and is similar to typical BFO. Theoretically, BAO possess an excellent ferroelectric value ($P_s \sim 90 \mu\text{C}/\text{cm}^2$) and high Curie temperature ($T_C \sim 530 \text{ }^\circ\text{C}$) [28]. BAO modified $\text{Bi}_{0.5}(\text{Na}, \text{K})_{0.5}\text{TiO}_3$ antiferroelectric ceramics possess excellent energy storage characteristics [29]. Hence, in this work, nonmagnetic Al was selected and substituted for Fe in BFO films via the spin coating method. The spin coating method is widely used because it is low cost [16]. The structure, morphology, optical absorption and ferroelectricity of the as-prepared films were all systematically studied. Optimized Al doping BFO films can be used in the construction of next generation environmentally friendly intensive nanodevices.

2. Experimental

2.1. Synthesis

Commercially available and analytical grade $\text{Bi}(\text{NO}_3)_3 \cdot 5\text{H}_2\text{O}$, $\text{Fe}(\text{NO}_3)_3 \cdot 9\text{H}_2\text{O}$, $\text{Al}(\text{NO}_3)_3 \cdot 9\text{H}_2\text{O}$, 2-methoxyethanol ($\text{C}_3\text{H}_8\text{O}_2$), glacial acetic acid (CH_3COOH), nitric acid (HNO_3), citric acid ($\text{C}_6\text{H}_8\text{O}_7$), glycol ($(\text{CH}_2\text{OH})_2$, EG), and ethanolamine ($\text{C}_2\text{H}_7\text{NO}$) were used as raw materials. Two kinds of precursors were prepared: one

was an aqueous solution of nitric acid (solvent I), and the other was a mixture of 2-methoxyethanol and acetic acid in a volume ratio of 3:1 (solvent II). Citric acid was used as a complexing agent in both solvents, and appropriate amounts of glycol and ethanolamine are added to stabilize the solution. Excess Bi (4 at.%) was used to compensate for volatilization. The concentration of cation (Bi^{3+} , Fe^{3+} , Al^{3+}) is about 0.5 mol/L, fluorine-doped tin oxide conductive glass (FTO, SnO_2 : F) were served as substrates. BiFeO_3 (BFO) and $\text{BiFe}_{0.96}\text{Al}_{0.04}\text{O}_3$ (BFAO) thin films were synthesized via spin coating. The precursor solvent was spin coated on FTO substrate with a maximum rotation speed of 4000 rpm for 15 s layer-by-layer, and then it was dried in an electric vacuum drying oven at 85 °C for 10 min. Subsequently, the FTO substrates with gel layers were pushed into a 550 °C-preheated muffle furnace for 10 min to remove the organic solvent. After 14 cycles of the coating/pyrolysis processes, the BFO or BFAO precursor films were sintered at 550 °C for 30 min in air. BFO and BFAO films that were prepared by an aqueous solution of nitric acid were denoted as BFO- I and BFAO- I, respectively, and those that were prepared using 2-methoxyethanol and glacial acetic acid were denoted as BFO- II and BFAO- II, respectively.

2.2. Characterization

Crystal structures of the thin films were analyzed from X-ray diffraction (XRD, D/max 200) measurements. Ultraviolet-visible spectrophotometry (UV-Vis, GBC Gintra-20) was used to record the absorption spectra. Field emission scanning electron microscopy (FE-SEM, TESCAN VEGA3) was employed to observe the microstructures (surface morphology and thickness) and energy dispersive spectroscopy (EDS, Thermo) to obtain surface element information of the sample. Raman spectra of the films were collected using a LabRAM HR Evolution (Horiba, France). X-ray photoelectron spectroscopy (XPS) was recorded on an ESCALAB 250xi (Thermo, USA) with Al $K\alpha$ radiation to determine the chemical states of samples, and the adventitious C1s peak at 284.8 eV was used to calibrate all other binding energies. The electrical properties (mainly P-E loops and leakage current density) were characterized using a ferroelectric test system (aix ACT). Before polarization measurement, several circular Pt upper electrodes with a diameter of 0.6 mm were deposited on the surface of films utilized ion sputtering with shadow masks.

3. Results and discussion

3.1. Structure and morphology

Typical XRD patterns of BFO thin films are shown in Fig. 1. All of the thin film samples have sharp diffraction peaks. Compared to the standard PDF (BiFeO₃: PDF#71-2494), it can be concluded that all of the thin film samples remained pure phase, and crystal structures of the samples could be indexed to distorted rhombohedral structure with space group *R3c*. In addition, some of the diffraction peaks do not correspond to BFO mainly correspond to conductive oxides (SnO₂: F) on the surface of the FTO substrate, and no secondary phases were observed in any of the samples.

To investigate the growth quality of Al-doped BFO films using two kinds of solvents, SEM was employed to directly observe the microstructures of the films. Fig. 2 shows SEM images of the surface of films. There are some pores on the surface of the BFO films prepared using the two solvents. The average grain size of BFO- I is the largest of all of the samples, and this was about 167.6 nm. Al doping refines the grain size, reduces pores, and increases the density of the film. The average grain size of the BFAO- I sample was about 120.7 nm. On the whole, the grain size of the BFO films that were prepared using the 2-methoxyethanol and glacial acetic acid solvent were more refined than those of the BFO films that were prepared by nitric acid solvent. The crystal sizes of BFO- II and BFAO- II films were 148.4 and 111.7 nm, respectively. At the same time, a cross-sectional sample of each film was prepared using liquid nitrogen embrittlement treatment, and SEM was used to observe the composition of the cross-section. There was an obvious interface (BFO/FTO) in the cross-section, as seen in Fig. 3. The thickness BFO- I film was maximum about 845.27 nm, the minimum thickness belonged to BFAO- II film was about 714.28 nm. The thickness values of BFAO- I and BFO- II are 818.16 and 770.73 nm, respectively. In the same solvent, Al doping results in a film that is more compact and has thinner thickness.

To further study the element distribution and content on the surface of the film sample, we carried out surface element scanning of the sample prepared with

2-methoxyethanol and glacial acetic acid as the solvent. Scanning results are shown in Fig. 4. Bi, Fe, O and Al elements with less content are evenly distributed on the surface of the BFAO- II sample. The atomic proportion that measured from the energy spectrum basically conforms to the proportion of metal ions in the preparation of raw materials, according to the atomic ratio of the element contents.

The elements information for the BFAO sample that was prepared with the 2-methoxyethanol and glacial acetic acid solvent were further studied using XPS. Fig. 5 shows XPS results for the BFAO- II sample. From the XPS map, the corresponding bond energy positions of Bi, Fe and O were clearly obtained. From the enlarged image, the two peaks are found near 160 eV, and these correspond to Bi 4f_{7/2} (158.6 eV) and Bi 4f_{5/2} (164.1 eV). The two peaks might be related to Bi-O-Fe and Bi-O-Al bonds in the oxygen octahedron and indicate that the valence of Bi in the sample is +3 [30]. Also, there are two peaks that correspond to Fe³⁺ that were observed via XPS: Fe 2p_{3/2} (710.3 eV) and Fe 2p_{1/2} (724.1 eV). These peaks indicate that Fe in the BFAO- II sample was mainly in the +3 valence, and this provides a new idea for introducing invariable valence Al (+3) to inhibit changes in the valence of Fe in BFO materials.

3.2. Raman and UV-Vis spectra

To further study the influences that Al doping and different solvents have on the structure of the film samples, Raman spectra were recorded of all the samples. BFO has a perovskite structure of the *R3c* space group. There are 27 kinds of phonon vibration modes that are produced by 10 atoms in the cell, which can be defined as $r_{opt} = 4A_1 + 5A_2 + 9E$. However, 5A₂ modes are not Raman active, and 9E modes are doubly degenerate. Fig. 6 depicts the Raman spectra of the film samples, these 13 Raman active vibration modes (4A₁ + 9E) [31] are seen in Fig. 6 (a). The ferroelectricity of BFO is usually attributed to E-1, E-2 and 4A₁. Low frequency modes (A₁-1 and A₁-2) and intermediate frequency modes are associated with Bi-O [32, 33]. Fig. 6 (b) is an enlarged view in the range of 60-250 cm⁻¹. There are four obvious Raman vibration modes in this low frequency region, E-1 (~ 70 cm⁻¹), A₁-1 (~ 140 cm⁻¹), A₁-2 (~ 170 cm⁻¹) and A₁-3 (~ 230 cm⁻¹). Also, an E-2 mode (~ 115 cm⁻¹)

corresponds to Fe. For Al-doped samples BFAO (I , II), A₁-1 and E-1 are narrower, and the strength of E-2 is weaker. Undoubtedly, Al doping leads to a certain anharmonic vibration of the lattice and weakens the vibration of Fe in the lattice. However, the A₁-3 mode corresponds to the octahedral structure of FeO₆, and Al doping enhances its strength. This indicates that the octahedral structure of FeO₆ is distorted; this gives rise to the Jahn-Teller effect, which is a result of Al doping [34]. These observations indicate that film samples that were prepared by two solvents introduce Al enter to BFO lattice.

The spin coating thin film is nanoscale and sensitive to optical signal. The UV-Vis absorption spectra of BFO (I , II) and BFAO (I , II) films were recorded, and the light absorption curves are shown in Fig. 7 (a). As seen in the absorption curves, the film samples mainly absorb 300-500 nm blue-green light, and the absorption peak of the film is at 450 nm for BFO (I , II). When 0.04-Al was introduced into the films, the absorption range of the BFAO films became wider. The absorption peak underwent a slight red shift, with the peak moving to the vicinity of 500 nm. Al doping improved the absorption and utilization ability of the visible light.

The band gap width (E_g) of each film sample was then calculated using the classical Tauc formula, as written in Eq. (1) [35]

$$(\alpha h\nu)^n = A(h\nu - E_g) \quad (1)$$

where α is the absorption coefficient that originates from measuring, h is Planck's constant ($h = 6.62607015 \times 10^{-34}$ J·s), ν is the photon frequency (test frequency), A is a constant, E_g is the bandgap, and n is the exponential coefficient that correlates to the nature of the E_g transition (direct E_g : $n = 2$). The $(\alpha h\nu)^2$ - $h\nu$ curves of the films were plotted in Fig. 7 (b). The values of the forbidden band width (E_g) of the BFO (I , II) and BFAO (I , II) samples are 2.28, 2.26, 2.17 and 2.21 eV, respectively. This work indicates that the E_g of BFO films can be adjusted by changing the preparation of the solvent or by introducing Al. Thus, these approaches improve the absorption ability of visible light, facilitate the application of BFO film in photocatalytic decomposition of methyl orange and other organic matters, and provide a new idea for photovoltaic

devices.

3.3 P-E loops and leakage current

The ferroelectric properties of BFO (I , II) and BFAO (I , II) samples were tested using an aix ACT system. As discussed in the previous section, SEM was used to test the thickness of BFO (I , II) and BFAO (I , II) samples. The test voltage (V) divided by the thickness of the film (d) can be converted into electric field strength ($E = V/d$). The P-E curves of BFO (I , II) and BFAO (I , II) samples are shown in Fig. 8. The residual polarization value ($+P_r$) of the BFO film that was prepared using nitric acid is about $10 \mu\text{C}/\text{cm}^2$, whereas the residual polarization values ($+P_r$) of BFO and BFAO samples prepared using 2-methoxyethanol and glacial acetic acid in positive electric field are $33.2 \mu\text{C}/\text{cm}^2$ and $57.6 \mu\text{C}/\text{cm}^2$, respectively. The hysteresis loop of BFO is not completely symmetrical, $2P_r$ ($+P_r$ add $-P_r$) and coercive field $2E_c$ ($+E_c$ add $-E_c$) were applied to describe the ferroelectricity. The $2P_r$ values are $21.1 \mu\text{C}/\text{cm}^2$ (BFO- I), $67.2 \mu\text{C}/\text{cm}^2$ (BFO- II), $16.7 \mu\text{C}/\text{cm}^2$ (BFAO- I), $111.2 \mu\text{C}/\text{cm}^2$ (BFAO- II), and the corresponding $2E_c$ are $1110 \text{ kV}/\text{cm}$, $959 \text{ kV}/\text{cm}$, $1228 \text{ kV}/\text{cm}$, and $1116 \text{ kV}/\text{cm}$, respectively. The results show that the ferroelectric properties of BFO films that were prepared using solvent- II show superior ferroelectric performances, and the $2P_r$ value of BFAO- II is about $110 \mu\text{C}/\text{cm}^2$. Al doping improves remanent polarization and leads to a higher coercive field. The enhanced ferroelectric behavior is attributable to well-distributed fine grains and to the film texture [36]. Zhang et al. [37] used spin coating method and prepared $\text{BiFe}_{0.95}\text{Al}_{0.05}\text{O}_3$ and $\text{BiFe}_{0.9}\text{Al}_{0.1}\text{O}_3$ thin films on Pt(111)/ $\text{TiO}_2/\text{SiO}_2/\text{Si}$ substrates, and the $2P_r$ values were $63 \mu\text{C}/\text{cm}^2$ and $54 \mu\text{C}/\text{cm}^2$, respectively. Excessive Al doping weakens the ferroelectric properties of BFO films, and this may be a result of the spontaneous polarization of BAO ($P_s \sim 90 \mu\text{C}/\text{cm}^2$), which is lower than BFO ($P_s \sim 150 \mu\text{C}/\text{cm}^2$), theoretically.

The leakage current curves of the film samples were then tested. The problem of high leakage always hinders the application of BFO film on commercialized devices. Fig. 9 (a) shows leakage current curves of the BFO (I , II) and BFAO (I , II) samples. The values of leakage current of the thin film samples prepared with nitric acid as the solvent were larger, and the test field was lower than that of the thin film

sample that were prepared with 2-methoxyethanol and glacial acetic acid as the solvent. The leakage of BFO- I was about 3×10^{-2} A/cm² at 150 kV/cm. However, the leakage of BFAO- II is about 1×10^{-3} A/cm² at 150 kV/cm and 1×10^{-2} A/cm² at 300 kV/cm. These test results are related to the quality of the thin films. The SEM images above also show that there are more pores in the two samples that were prepared using the nitric acid precursor, and the density of the thin film is lower than that of the BFO- II and BFAO- II films.

To study the conduction mechanism of the sample, we calculated the slope to describe the evolution of the leakage current with the field strength. The logJ-logE curves in the positive bias region are displayed in Fig. 9 (b). According to the slopes (S) obtained with different values of electric field strength (E), all of the logJ-logE curves can be divided into three stages. The slope of the first stage is about 1.5, and this indicates that the Ohmic conduction mechanism is dominant under a low electric field. Under a higher electric field, the value of the slope increases, and the control conductivity mechanism is gradually evolving. In the third stage, the slopes of BFAO film that was prepared with each of two solutions are about 3. At higher electric field the dominant conduction mechanism of Al doped film is Schottky conductivity mechanism. The evolution of the conductivity mechanism indicates that the concentration of defective dipoles changes. The sharp increase in the slope may be a result of the complete filling of injected electrons by an effective trap related to the defects [38]. Al doping may reduce the concentration of oxygen vacancies. The slope of the undoped sample is lower; however, the leakage current value is larger than Al-doped films. The transition period from the Ohmic contact to the Schottky conduction mechanism of undoped BFO is longer, and the test electric field cannot continue to increase because of the poor quality of the film.

4. Conclusions

BiFeO_3 and $\text{BiFe}_{0.96}\text{Al}_{0.04}\text{O}_3$ thin films were successfully synthesized via the sol-gel method and spin coating on FTO substrates. All of the samples have rhombohedral structure with the $R3c$ space group. Al doping gives rise to the Jahn-Teller effect with

some structural distortion of the BFO film; it also leads to grain refinement and improved comprehensive properties for high density. Average grain sizes of the samples are 167.6 (BFO-I), 148.4 (BFO-II), 120.7 (BFAO-I) and 111.7 (BFAO-II) nm, and the corresponding thickness of these samples are 845.27, 770.73, 818.16, and 714.28 nm, respectively. The leakage cures of the films were dominated by the Ohmic and Schottky conduction mechanisms. BFAO- II possesses excellent ferroelectricity ($2P_r \sim 110 \mu\text{C}/\text{cm}^2$), and its leakage current density ($\sim 1 \times 10^{-2} \text{ A}/\text{cm}^2$ at 300 kV/cm) is lower than that of undoped BFO films (BFO (I , II)). The E_g values of samples are 2.28 (BFO-I), 2.26 (BFO-II), 2.17 (BFAO-I), and 2.21 (BFAO-II) eV. This work provides a new idea for the application of BFAO films in photocatalysis and photovoltaic devices.

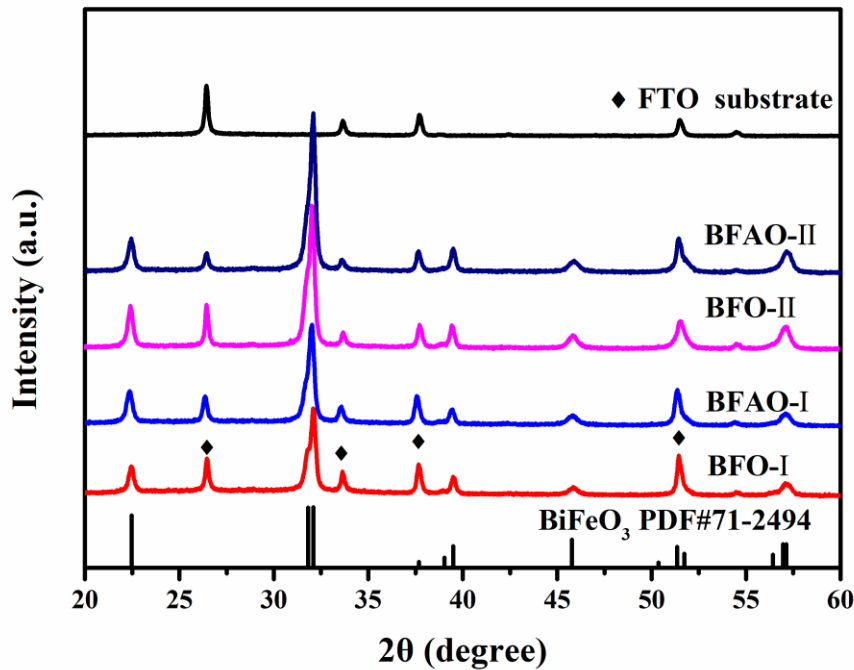


Fig. 1 XRD of BFO (I , II) and BFAO (I , II) films.

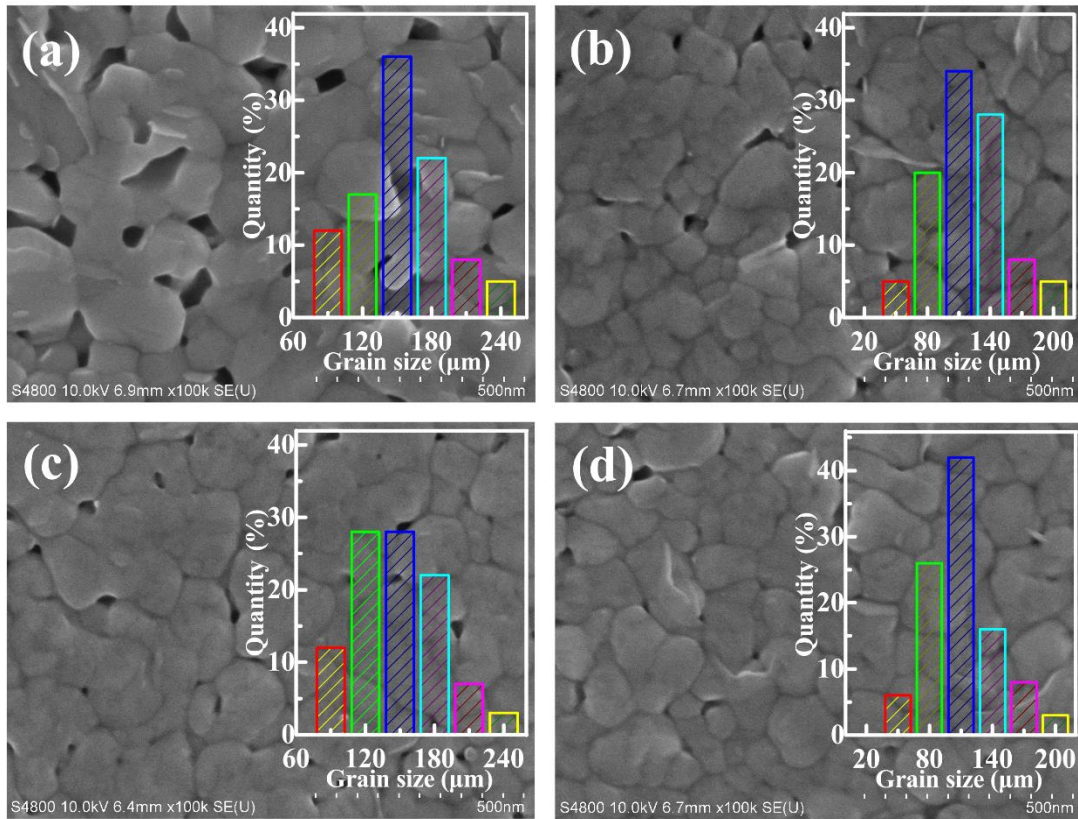


Fig. 2 Surface SEM images of BFO (I , II) and BFAO (I , II) films.

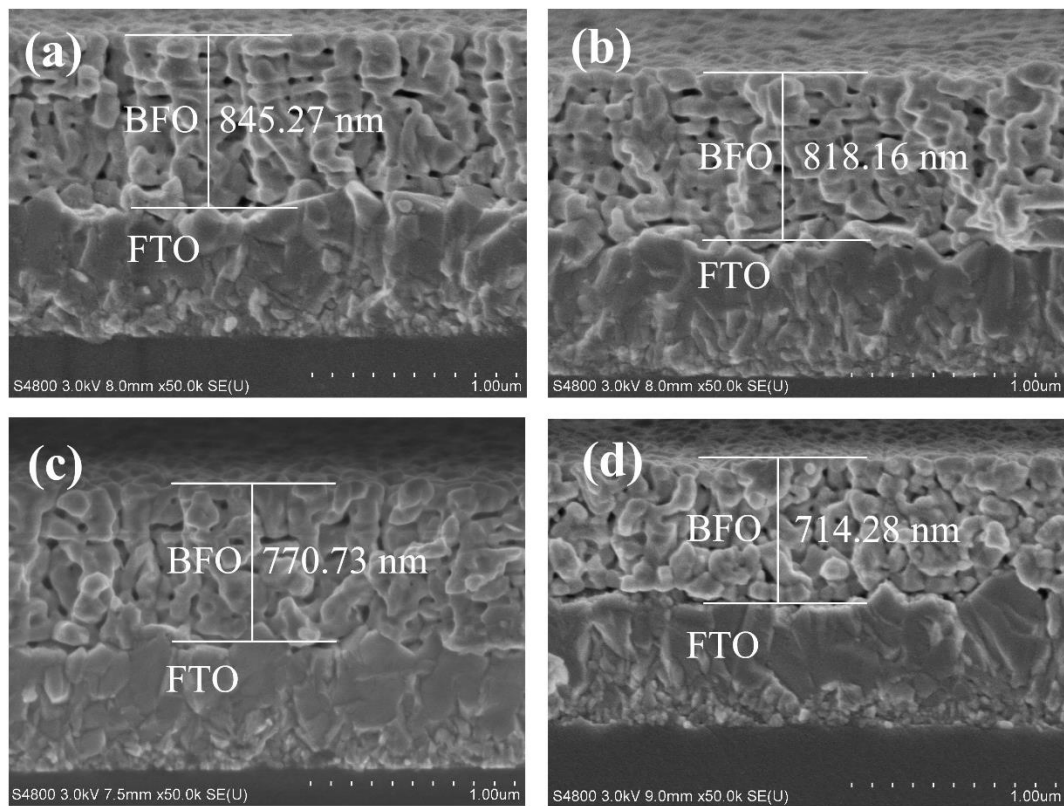


Fig. 3 Section SEM images of BFO (I , II) and BFAO (I , II) films.

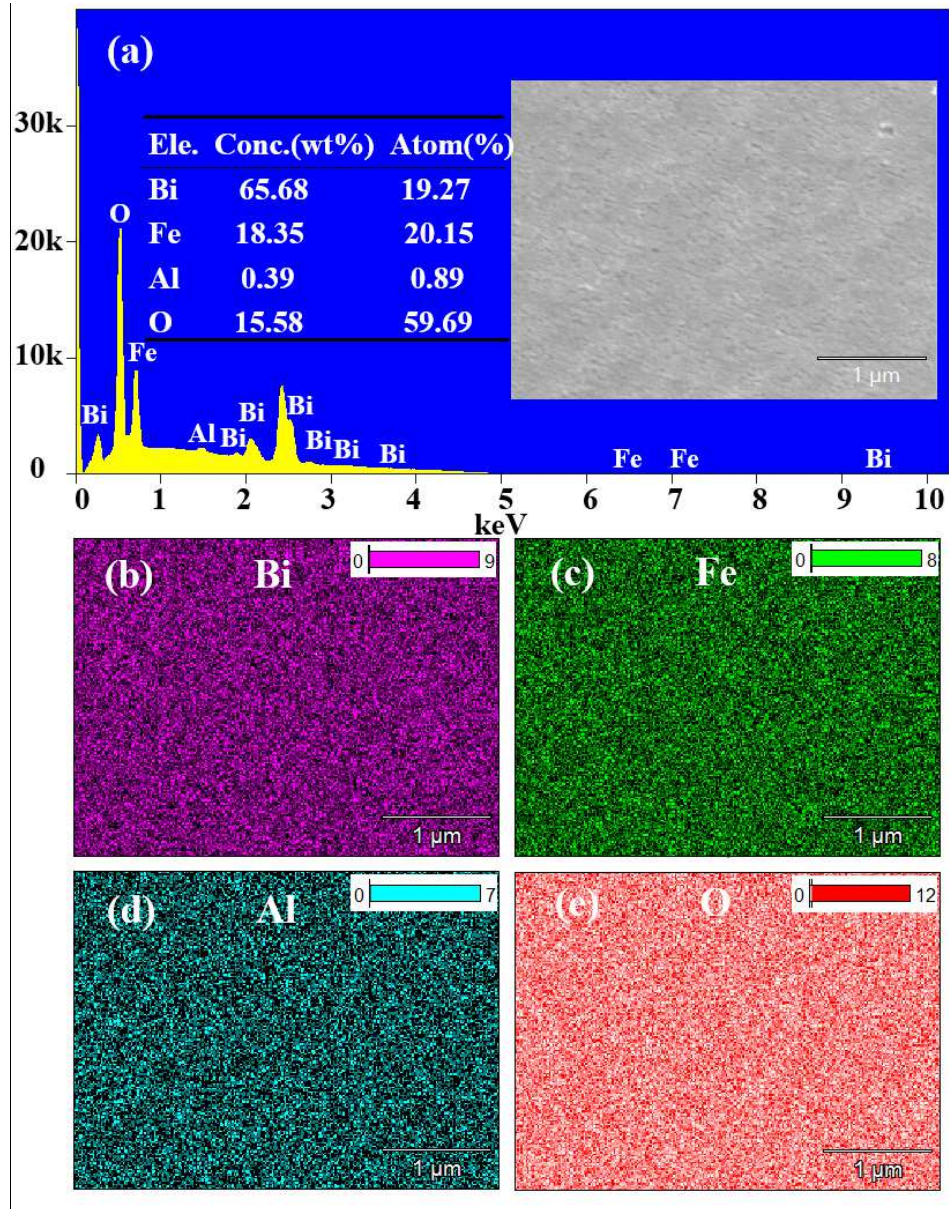


Fig. 4 Surface EDS and mapping of the BFAO- II sample, (a) EDS of BFAO- II film, (b-e) element mapping for Bi, Fe, Al and O, respectively.

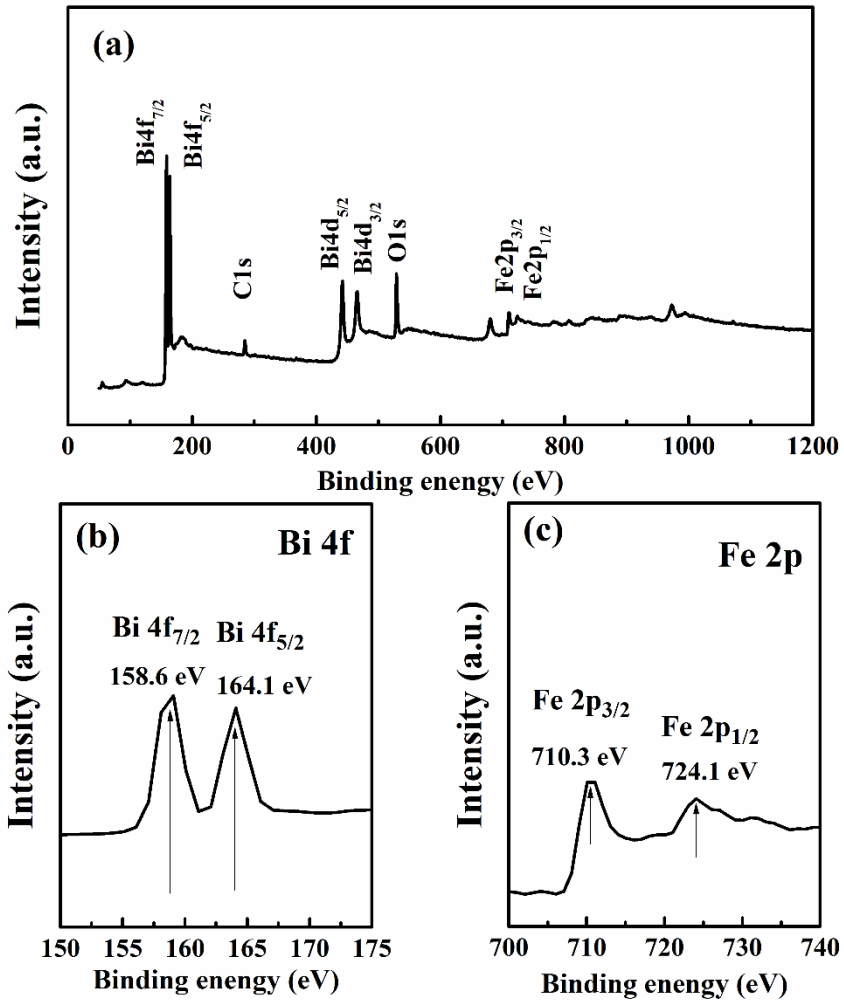


Fig. 5 Surface XPS of the BFAO- II sample (a) 0-1200 eV, (b) 150-175 eV, and (c) 700-740 eV.

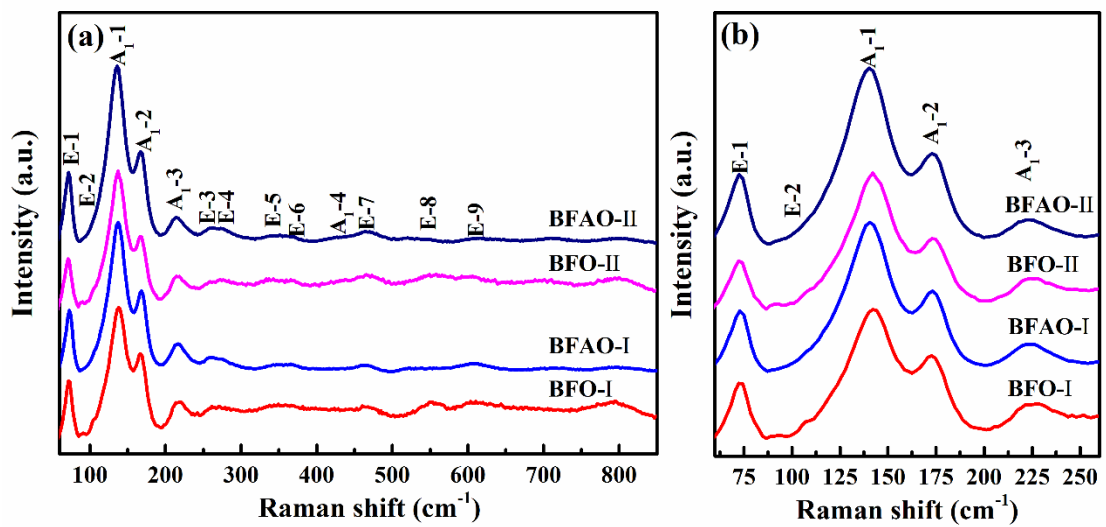


Fig. 6 Raman spectra of BFO (I , II) and BFAO (I , II) films: (a) 60-800 cm^{-1} and (b) 60-250 cm^{-1} .

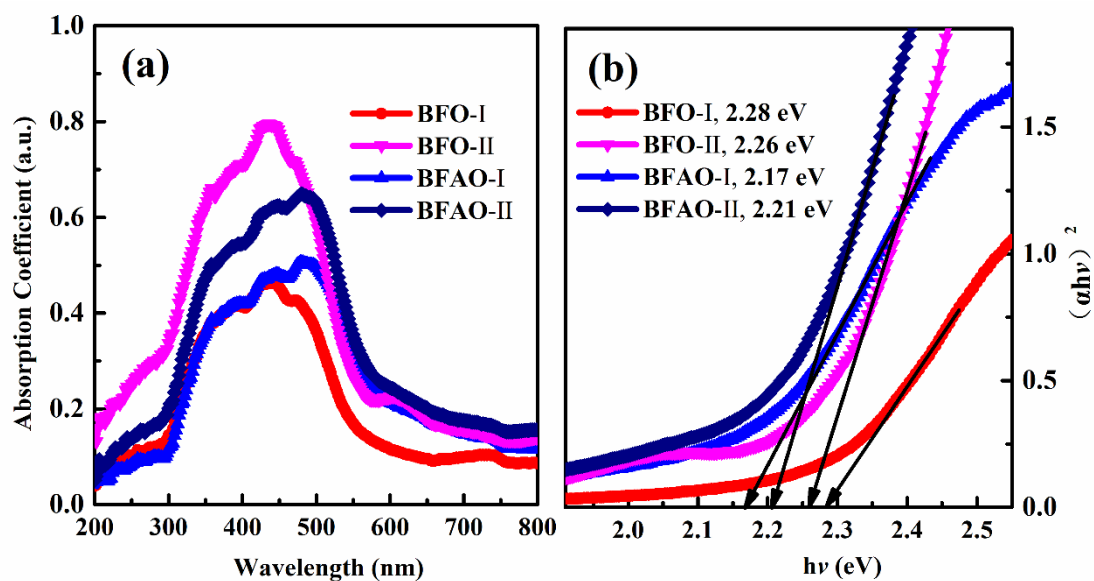


Fig. 7. (a) UV-Vis absorption spectra of BFO (I , II) and BFAO (I , II) films and (b) $(\alpha h\nu)^2$ - $h\nu$ curves of BFO (I , II) and BFAO (I , II) films.

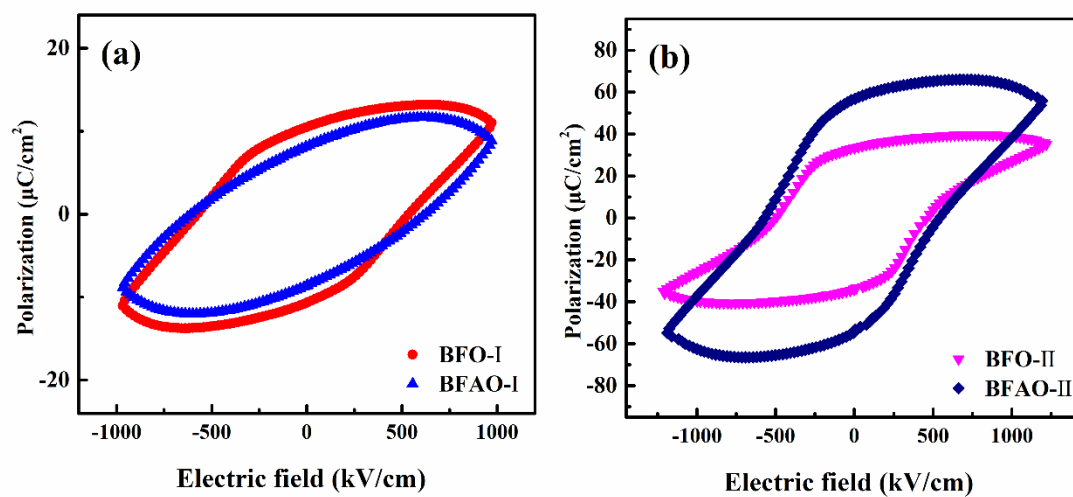


Fig. 8 P-E curves of BFO (I , II) and BFAO (I , II) films: (a) for BFO- I and BFAO- I and (b) for BFO- II and BFAO- II.

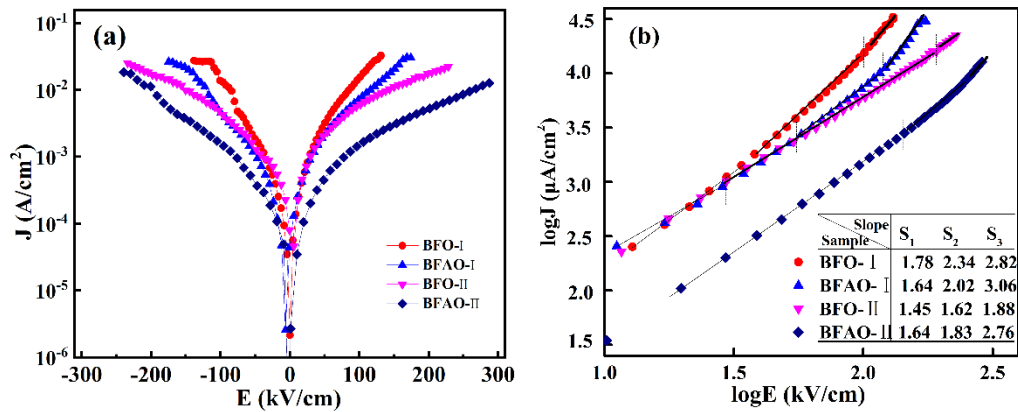


Fig. 9 Leakage current curves of BFO (I , II) and BFAO (I , II) films: (a) for J-E and (b) for logJ-logE.

References

- 1 T. Lottermoser, T. Lonkai, U. Amann, D. Hohlwein, J. Ihringer, M. Fiebig, Magnetic phase control by an electric field, *Nature* 430 (2004) 541-544
- 2 J. Wang, J.B. Neaton, H. Zheng, V. Nagarajan, S.B. Ogale, B. Liu, D. Viehland, V. Vaithyanathan, D.G. Schlom, U.V. Waghmare, Epitaxial BiFeO₃ multiferroic thin film heterostructures, *Cheminform* 299 (2003) 1719-1722
- 3 R.Q. Yin, B.W. Dai, P. Zheng, J.J. Zhou, W.F. Bai, F. Wen, J.X. Deng, L. Zheng, J. Du, H.B. Qin, Pure-phase BiFeO₃ ceramics with enhanced electrical properties prepared by two-step sintering, *Ceram. Int.* 43 (2017) 6467-6471
- 4 A. Azam, A. Jawad, A.S. Ahmed, M. Chaman, A.H. Naqvi, Structural, optical and transport properties of Al³⁺ doped BiFeO₃ nanopowder synthesized by solution combustion method, *J. Alloy. Compod.* 509 (2011) 2909-2913
- 5 T.J. Park, G.C. Papaefthymiou, A.J. Viescas, A.R. Moodenbaugh, S.S. Wong, Size-dependent magnetic properties of single-crystalline multiferroic BiFeO₃ nanoparticles, *Nano Lett.* 7 (2007) 766-772
- 6 F.G. Figueiras, D. Dutta, N.M. Ferreira, F.M. Costa, M.P.F. Graça, M.A. Valente, Multiferroic interfaces in bismuth ferrite composite fibers grown by laser floating zone technique, *Mater. Des.* 90 (2016) 829-833
- 7 Y.H. Chu, Q. Zhan, L.W. Martin, M.P. Cruz, P.L. Yang, G.W. Pabst, F. Zavaliche, S.Y. Yang, J.X. Zhang, L.Q. Chen, D.G. Schlom, I.N. Lin, T.B. Wu, R. Ramesh, Nanoscale domain control in multiferroic BiFeO₃ thin films, *Adv. Mater.* 18 (2010) 2307-2311
- 8 M.M. Kumar, V.R. Palkar, K. Srinivas, S.V. Suryanarayana, Ferroelectricity in a pure BiFeO₃ ceramic, *Appl. Phys. Lett.* 76 (2000) 2764-2766
- 9 W. Eerenstein, N.D. Mathur, J.F. Scott, Multiferroic and magnetoelectric materials, *Nature* 442 (2006) 759-765

- 10 G. Catalan, J.F. Scott, Physics and applications of bismuth ferrite, *Adv. Mater.* 21 (2010) 2463-2485
- 11 D. Sando, A. Barthélémy, M. Bibes, BiFeO₃ epitaxial thin films and devices: past, present and future, *J. Phys.-Condens. Mat.* 26 (2014) 473201
- 12 Y.P. Wang, L. Zhou, M.F. Zhang, X.Y. Chen, J.M. Liu, Z.G. Liu, Room-temperature saturated ferroelectric polarization in BiFeO₃ ceramics synthesized by rapid liquid phase sintering, *Appl. Phys. Lett.* 84 (2004) 1731-1733
- 13 R. Mazumder, D. Chakravarty, D. Bhattacharya, A. Sen, Spark plasma sintering of BiFeO₃, *Mater. Res. Bull.* 44 (2009) 555-559
- 14 M.H. Lee, D.J. Kim, J.S. Park, S.W. Kim, T.K. Song, M.H. Kim, W.J. Kim, D. Do, I.K. Jeong, High-performance lead-free piezoceramics with high curie temperatures, *Adv. Mater.* 27 (2016) 6976-6982
- 15 C.J. Cheng, D. Kan, S.H. Lim, W.R. McKenzie, P.R. Munroe, L.G. Salamanca-Riba, R.L. Withers, I. Takeuchi, V. Nagarajan, Structural transitions and complex domain structures across a ferroelectric-to-antiferroelectric phase boundary in epitaxial Sm-doped BiFeO₃ thin films, *Phys. Rev. B* 80 (2009) 014109
- 16 X. Xue, G.Q. Tan, H.J. Ren, A. Xia, Structural, electric and multiferroic properties of Sm-doped BiFeO₃ thin films prepared by the sol-gel process, *Ceram. Int.* 39 (2013) 6223-6228
- 17 M. Muneeswaran, S.H. Lee, D.H. Kim, B.S. Jung, S.H. Chang, J.W. Jang, B.C. Choi, J.H. Jeong, Structural, vibrational, and enhanced magneto-electric coupling in Ho-substituted BiFeO₃, *J. Alloy. Compound.* 750 (2018) 276-285
- 18 D. Lee, M.G. Kim, S. Ryu, H.M. Jang, Epitaxially grown La-modified BiFeO₃ magnetoferroelectric thin films, *Appl. Phys. Lett.* 86 (2005) 222903
- 19 G.D. Hu, X. Cheng, W.B. Wu, C.H. Yang, Effects of Gd substitution on structure and ferroelectric properties of BiFeO₃ thin films prepared using metal organic decomposition, *Appl. Phys. Lett.* 91 (2007) 232909
- 20 D. Kan, L. Pálová, V. Anbusathaiyah, C.J. Cheng, S. Fujino, V. Nagarajan, K.M. Rabe, I. Takeuchi, Universal behavior and electric-field-induced structural transition in rare-earth-substituted BiFeO₃, *Adv. Funct. Mater.* 20 (2010) 1108-1115
- 21 S.W. Kim, M.H. Lee, H.I. Choi, D.J. Kim, J.S. Park, M.H. Kim, T.K. Song, D. Do, W.J. Kim, Leakage current behaviors of SrTiO₃ capped Mn-doped polycrystalline BiFeO₃ thin film, *Ferroelectrics* 454 (2013):19-22
- 22 J.G. Wu, J. Wang, D.Q. Xiao, J.G. Zhu, Mn⁴⁺: BiFeO₃/Zn²⁺: BiFeO₃ bilayered thin films of (1 1 1) orientation, *Appl. Surf. Sci.* 257 (2011) 7226-7230
- 23 N.N. Rong, M.S. Chu, Y.L. Tang, C. Zhang, X. Cui, H.H. He, Y.H. Zhang, Improved photoelectrocatalytic properties of Ti-doped BiFeO₃ films for water oxidation, *J. Mater. Sci.* 51 (2016) 5712-5723
- 24 F. Fan, C.L. Chen, B.H. Luo, K.X. Jin, The electric transport properties of Al-doped ZnO/BiFeO₃/ITO glass heterostructure, *J. Appl. Phys.* 109 (2011) 461-464.

- 25 J.F. Scott, *Ferroelectric Memories*, Springer, 2000
- 26 K. Ujimoto, T. Yoshimura, A. Ashida, N. Fujimura, Direct piezoelectric properties of (100) and (111) BiFeO₃ epitaxial thin films, *Appl. Phys. Lett.* 100 (2012) 102901
- 27 J.X. Zhang, Q. He, M. Trassin, W. Luo, D. Yi, M. D. Rossell, P. Yu, L. You, C.H. Wang, C.Y. Kuo, Microscopic origin of the giant ferroelectric polarization in tetragonal-like BiFeO₃, *Phys. Rev. Lett.* 107 (2011) 147602
- 28 J. Zylberberg, A.A. Belik, E. Takayama-Muromachi, Z.G. Ye, Bismuth aluminate: a new high-T_c lead-free piezo-/ferroelectric, *Chem. Mater.* 19 (2007) 6385-6390
- 29 Z.L. Yu, Y.F. Liu, M.Y. Shen, H. Qian, F.F. Li, Y.N. Lyu, Enhanced energy storage properties of BiAlO₃ modified Bi_{0.5}Na_{0.5}TiO₃-Bi_{0.5}K_{0.5}TiO₃ lead-free antiferroelectric ceramics, *Ceram. Int.* 43 (2017) 7653-7659
- 30 Z. Quan, W. Liu, H. Hu, S. Xu, B. Sebo, G.J. Fang, M.Y. Li, and X.Z. Zhao, Microstructure, electrical and magnetic properties of Ce-doped BiFeO₃ thin films, *J. Appl. Phys.* 104 (2008) 590-599
- 31 J. Wei, C. Wu, Y. Liu, Y. Guo, T. Yang, D. Wang, Z. Xu, R. Haumon, Structural distortion, spin-phonon coupling, interband electronic transition, and enhanced magnetization in rare-earth-substituted bismuth ferrite, *Inorg. Chem.* 56 (2017) 8964-8974
- 32 A. Benali, B.M.G. Melo, P.R. Prezas, M. Bejar, E. Dhahri, M.A. Valente, M.P.F. Graca, B.A. Nogueira, B.F.O. Costa, Structural, morphological, raman and ac electrical properties of the multiferroic sol-gel made Bi_{0.8}Er_{0.1}Ba_{0.1}Fe_{0.96}Cr_{0.02}Co_{0.02}O₃ material, *J. Alloy. Compound.* 775 (2018) 304-315
- 33 P.C. Sati, M. Kumar, S. Chhoker, M. Jewariya, Influence of Eu substitution on structural, magnetic, optical and dielectric properties of BiFeO₃ multiferroicceramics, *Ceram. Int.* 41 (2015) 2389-2398
- 34 L.Y. Chang, C.S. Tu, P.Y. Chen, C.S. Chen, V.H. Schmidt, H.H. Wei, D.J. Huang, T.S. Chan, Raman vibrations and photovoltaic conversion in rare earth doped (Bi_{0.93}RE_{0.07})FeO₃ (RE = Dy, Gd, Eu, Sm) ceramics, *Ceram. Int.* 42 (2016) 834-842
- 35 J. Tauc, *Amorphous and liquid semiconductors*, Plenum, New York, (1974) pp.171
- 36 G. Dong, G. Tan, Y. Luo, Y. Luo, W. Liu, H. Ren, A. Xia, Structural transformation and multiferroic properties of single-phase Bi_(0.89)Tb_(0.11)Fe_(1-x)Mn_xO₃ thin films, *Appl. Surf. Sci.* 290 (2014) 280-286
- 37 D.H. Zhang, P. Shin, X.Q. Wu, W. Ren, Structural and electrical properties of sol-gel-derived Al-doped bismuth ferrite thin films, *Ceram. Int.* 39 (2013) S461-S464
- 38 Y. Dai, Q. Gao, C. Cui, L. Yang, C. Li, X. Li, Role of ferroelectric/ferromagnetic layers on the ferroelectric properties of magnetoelectric composite films derived by chemical solution deposition, *Mater. Res. Bull.* 99 (2018) 424-428

Figures

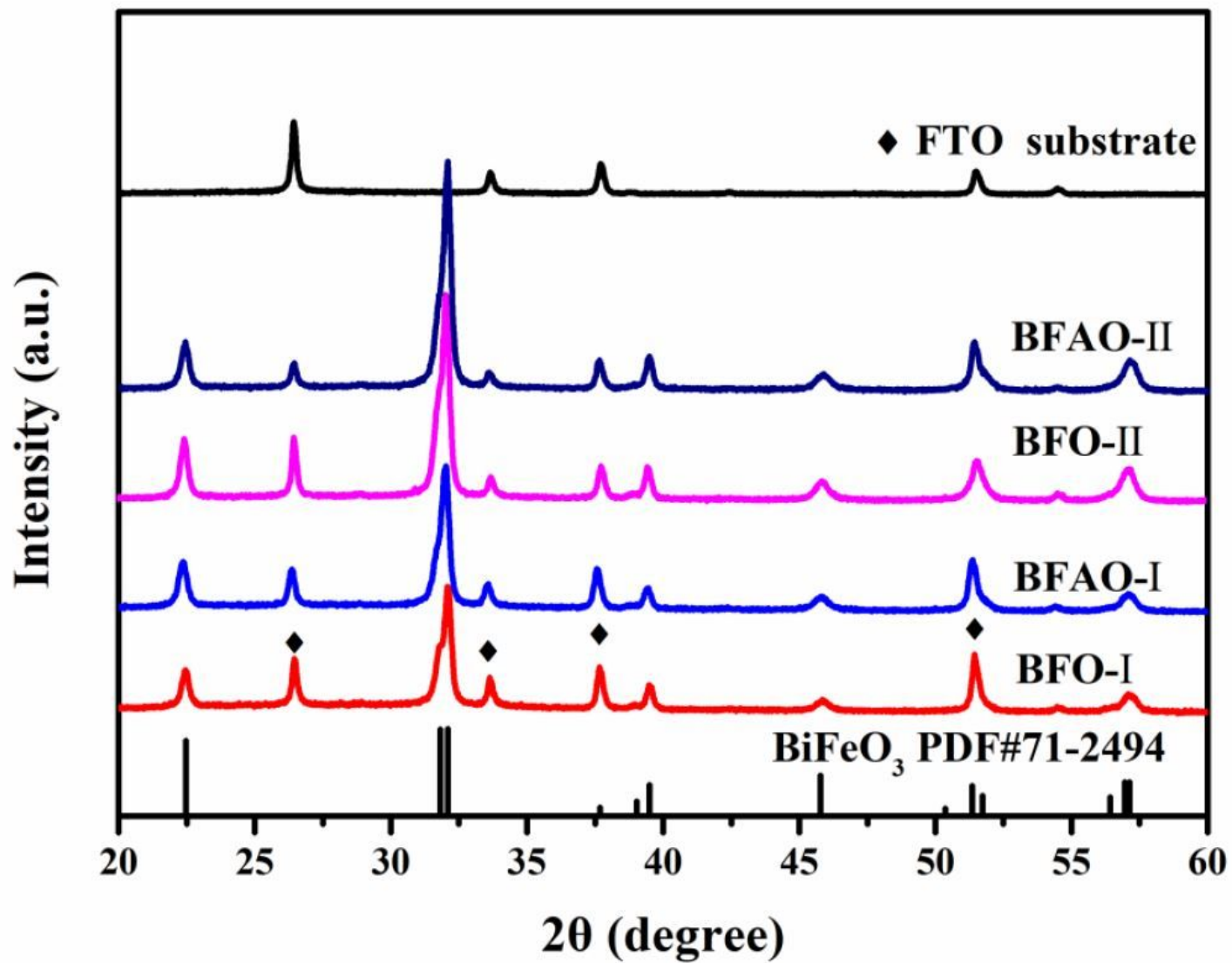


Figure 1

XRD of BFO (□, □) and BFAO (□, □) films.

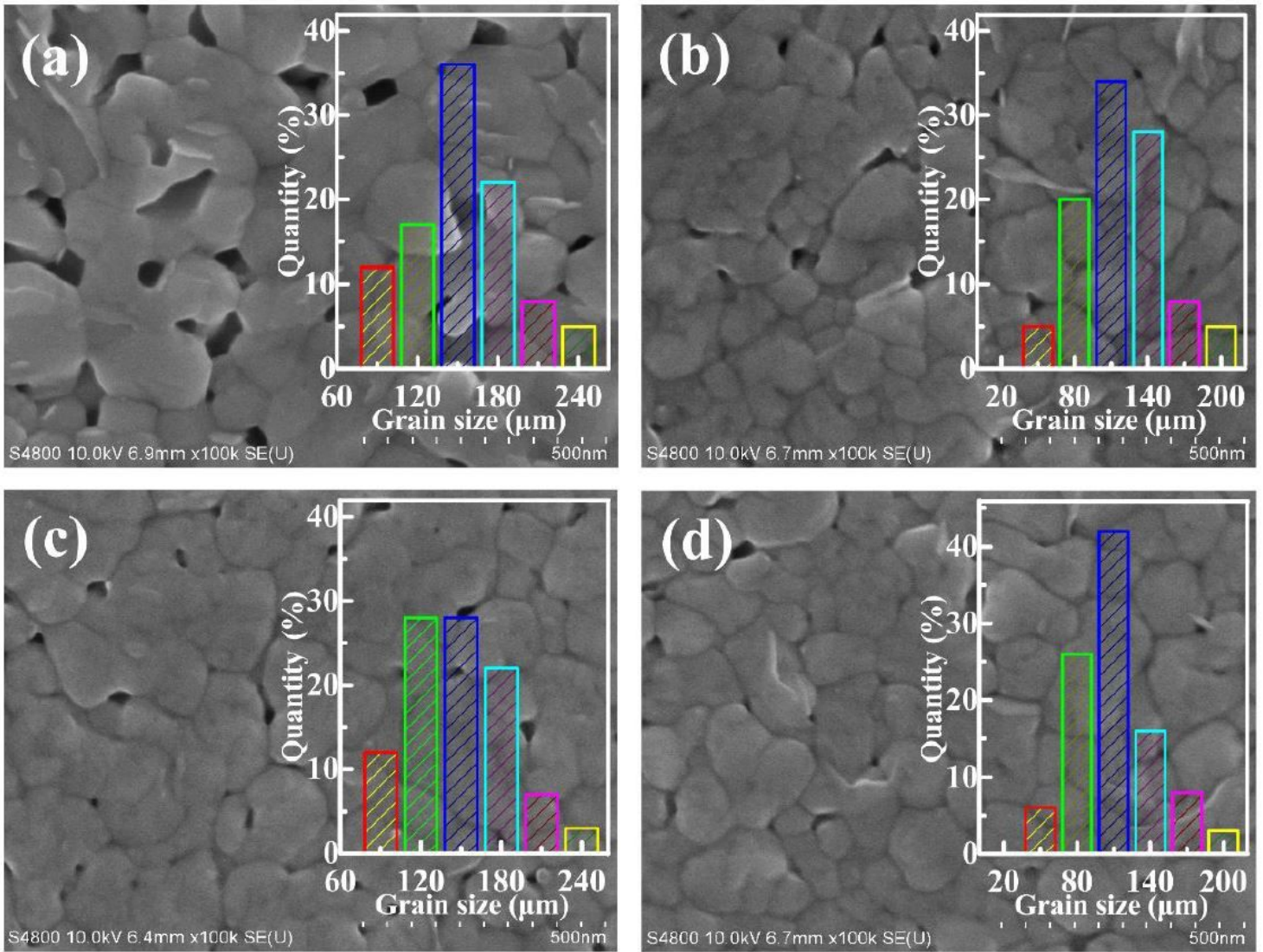


Figure 2

Surface SEM images of BFO (a, b) and BFAO (c, d) films.

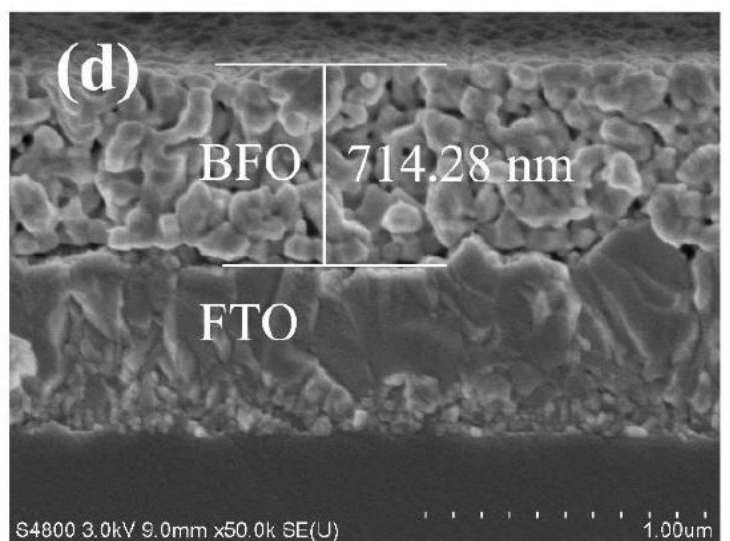
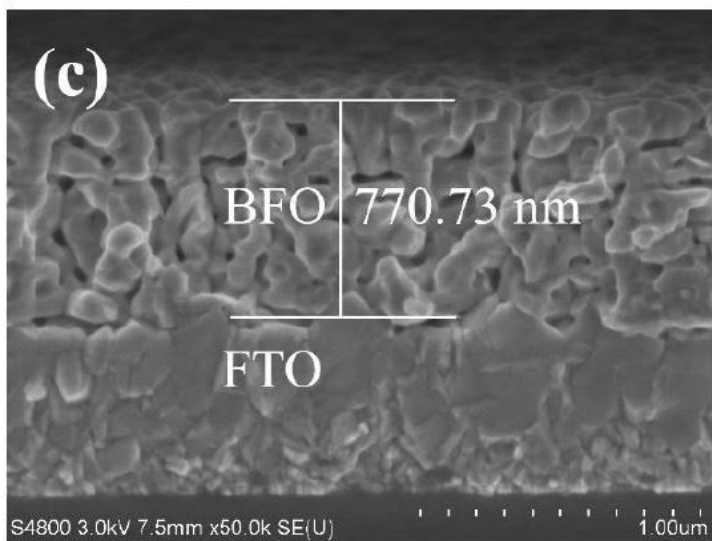
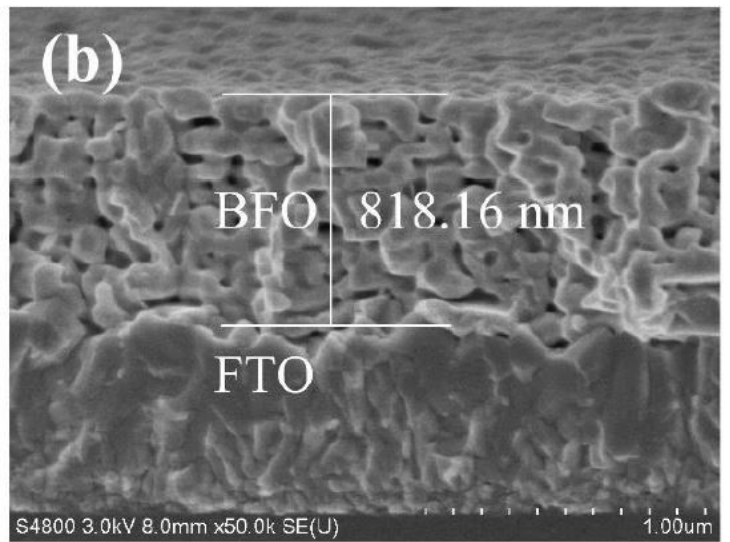
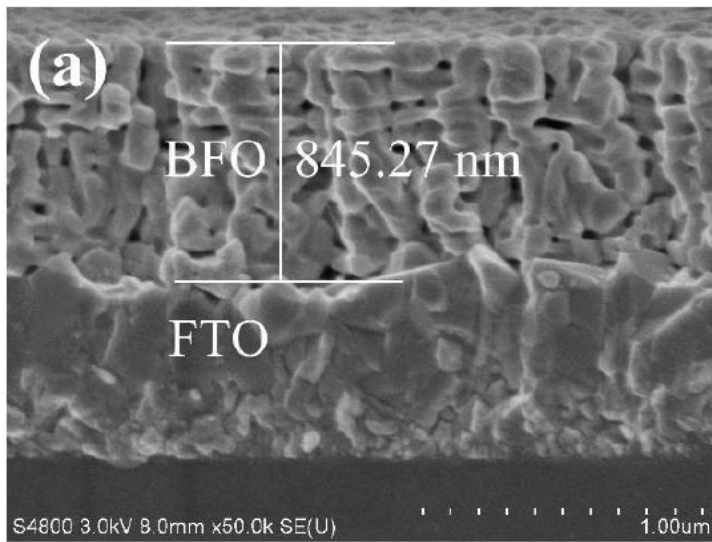


Figure 3

Section SEM images of BFO (a, b) and BFAO (c, d) films.

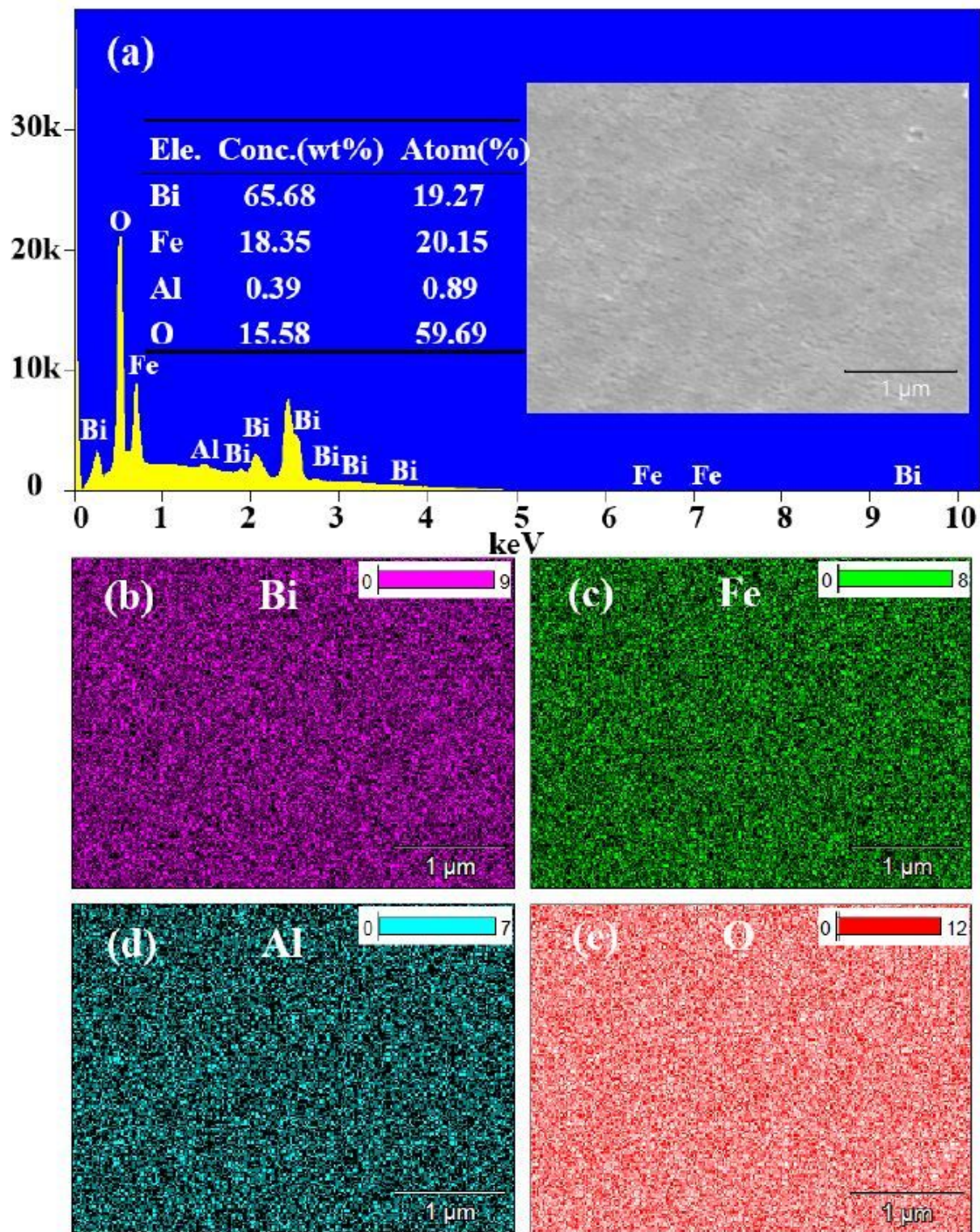


Figure 4

Surface EDS and mapping of the BFAO- δ sample, (a) EDS of BFAO- δ film, (b-e) element mapping for Bi, Fe, Al and O, respectively.

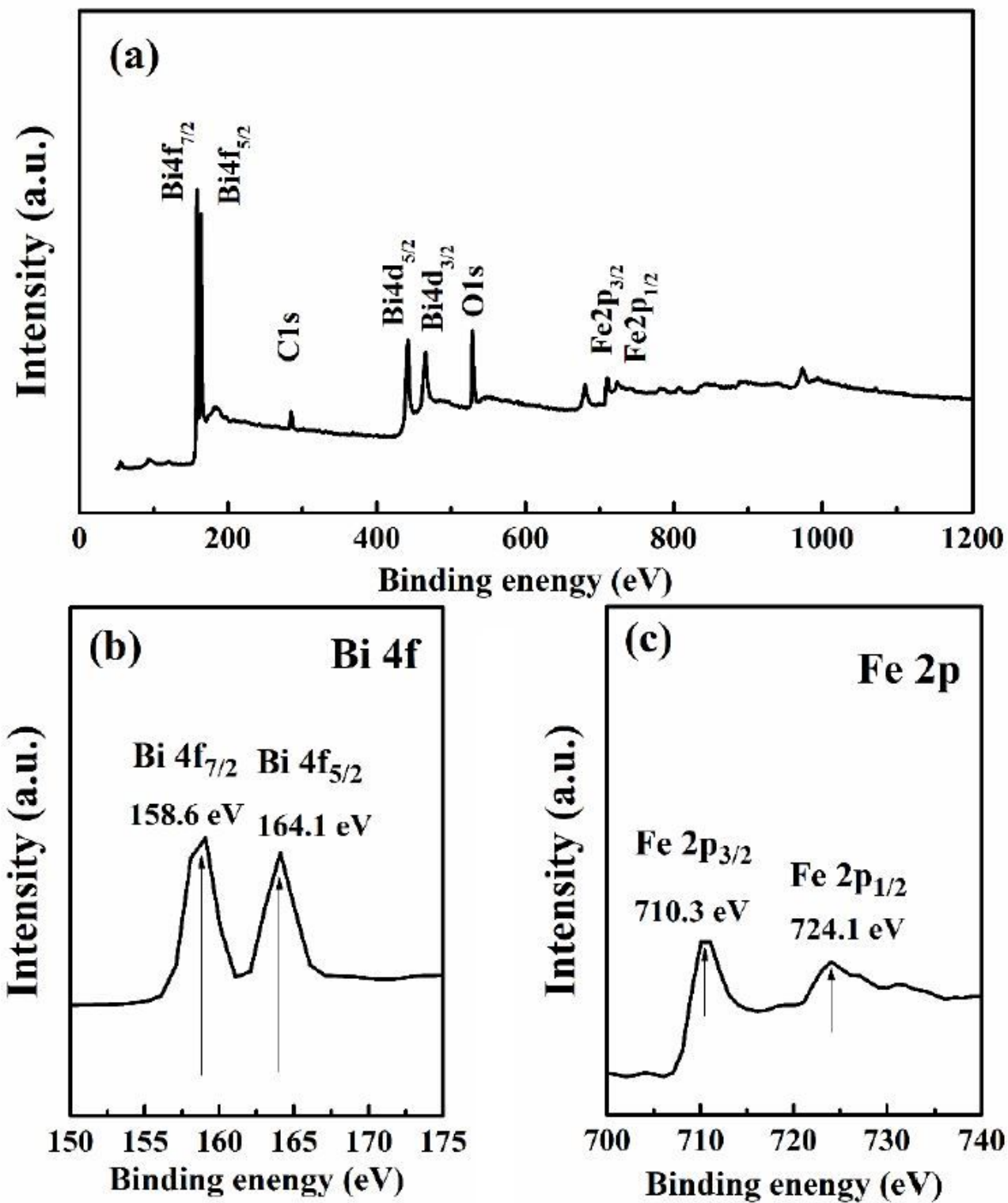


Figure 5

Surface XPS of the BFAO- δ sample (a) 0-1200 eV, (b) 150-175 eV, and (c) 700-740 eV.

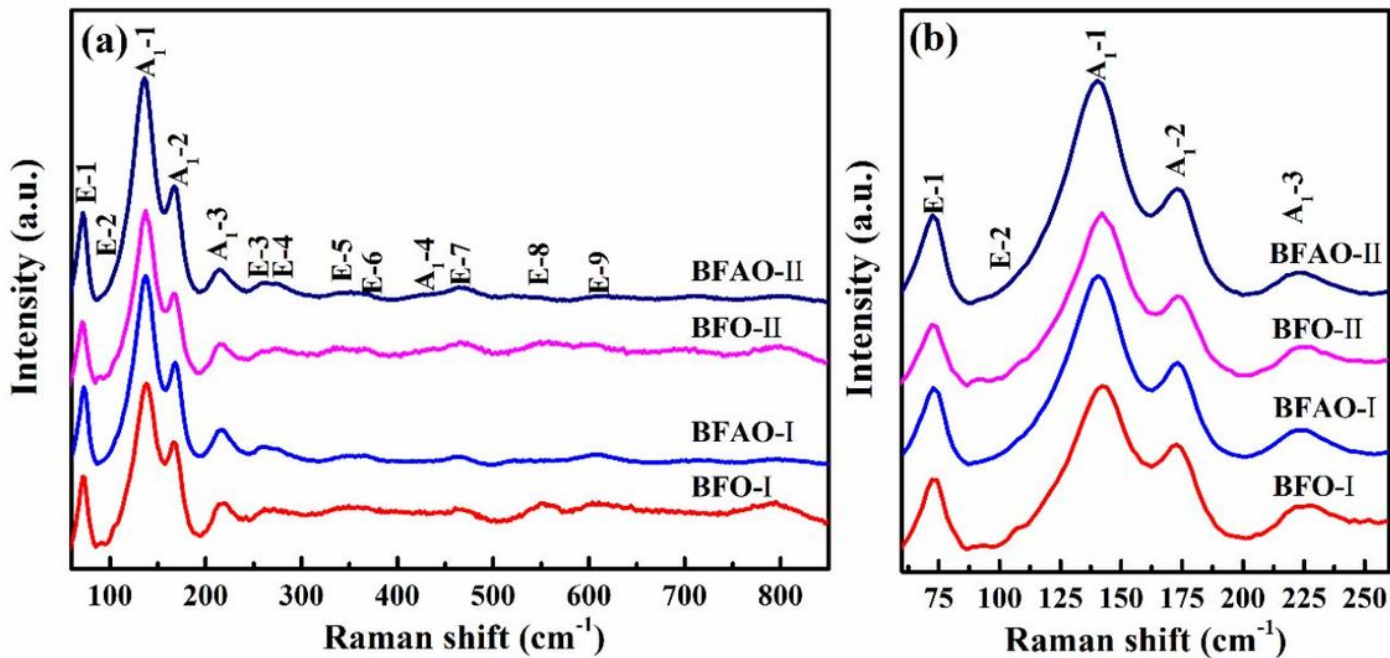


Figure 6

Raman spectra of BFO (□, □) and BFAO (□, □) films: (a) 60-800 cm⁻¹ and (b) 60-250 cm⁻¹.

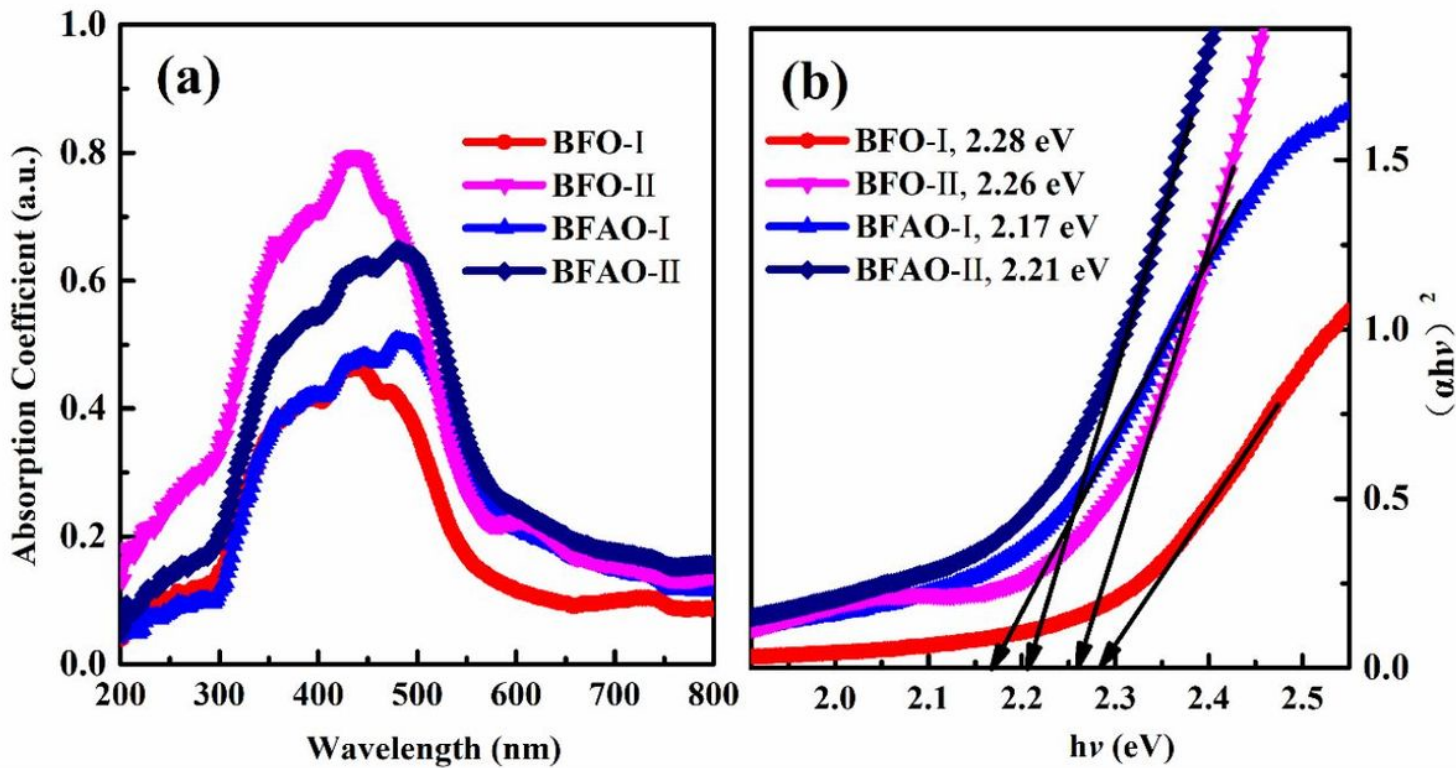


Figure 7

(a) UV-Vis absorption spectra of BFO (□, □) and BFAO (□, □) films and (b) $(\alpha h\nu)^2$ vs $h\nu$ curves of BFO (□, □) and BFAO (□, □) films.

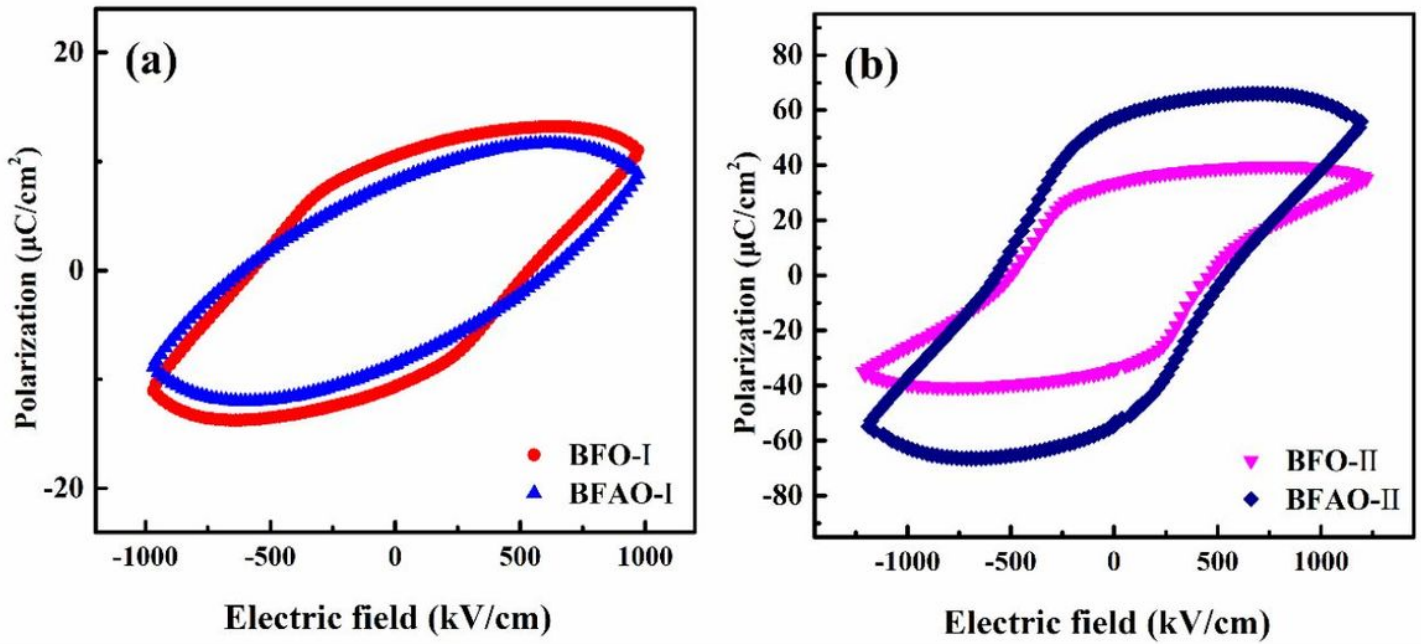


Figure 8

P-E curves of BFO (□, □) and BFAO (□, □) films: (a) for BFO-□ and BFAO-□ and (b) for BFO-□ and BFAO-□.

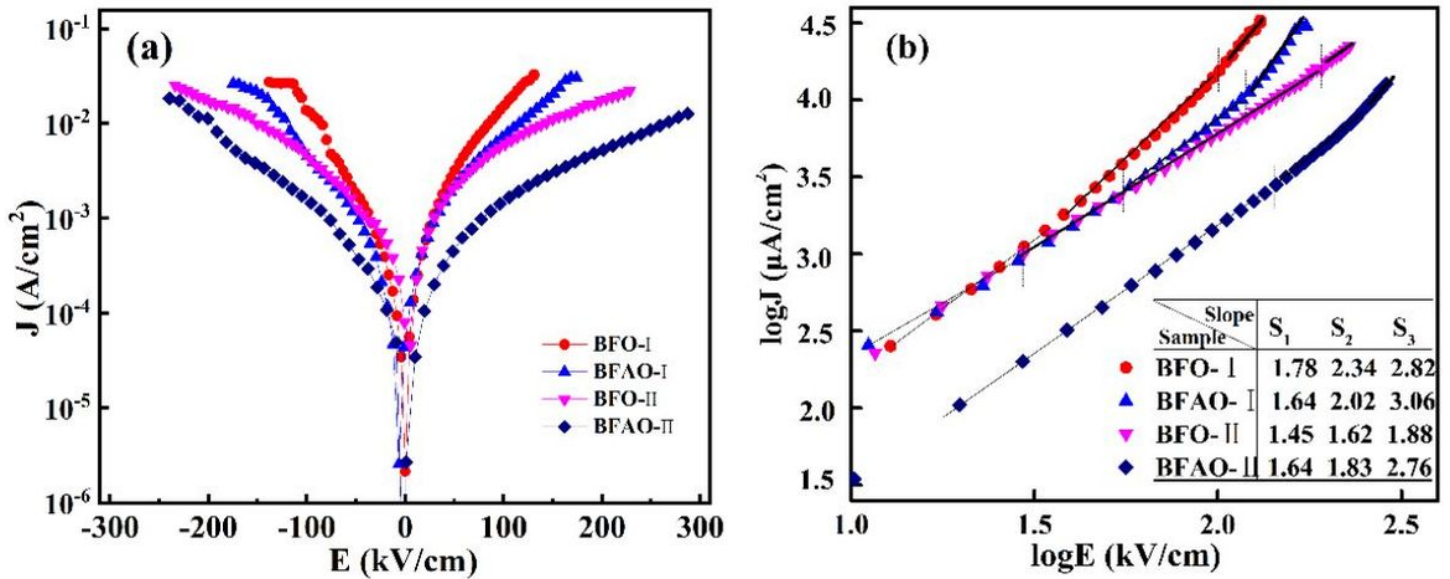


Figure 9

Leakage current curves of BFO (□, □) and BFAO (□, □) films: (a) for J-E and (b) for $\log J$ - $\log E$.